Cell Reports

Report

Circuit reorganization in the *Drosophila* mushroom body calyx accompanies memory consolidation

Graphical abstract

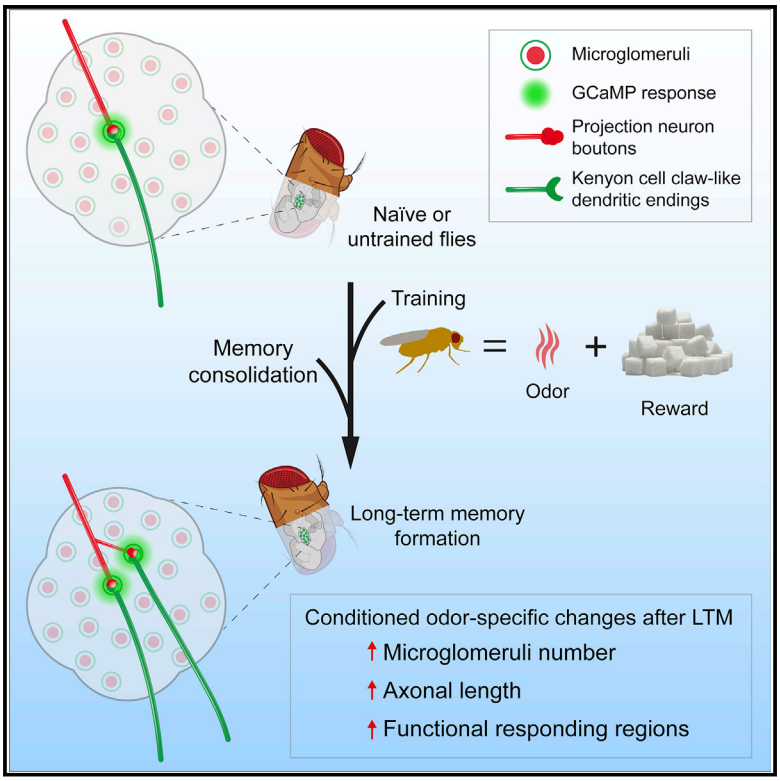

Highlights

- Synaptic microglomeruli linked to a specific odor can be identified in *Drosophila*
- Microglomeruli represent complex microcircuits involving different types of neurons
- Long-term memory results in increased microglomeruli in an input-specific manner
- Newly formed microglomeruli participate in conditioned odor representation

Authors

Lothar Baltruschat, Luigi Prisco, Philipp Ranft, J. Scott Lauritzen, André Fiala, Davi D. Bock, Gaia Tavosanis

Correspondence

gaia.tavosanis@dzne.de

In brief

Baltruschat et al. investigate structural modifications upon memory consolidation in a center essential for olfactory memory in *Drosophila*, in which second- and third-order neurons connect via synaptic microglomeruli. Although short-term memory reveals no evidence of structural plasticity, appetitive long-term memory is associated with increased microglomeruli in an input-specific manner.

Baltruschat et al., 2021, Cell Reports *34*, 108871
March 16, 2021
https://doi.org/10.1016/j.celrep.2021.108871

CellPress

Cell Reports

CellPress
OPEN ACCESS

Report

Circuit reorganization in the *Drosophila* mushroom body calyx accompanies memory consolidation

Lothar Baltruschat,[1,6] Luigi Prisco,[1,6] Philipp Ranft,[1,6] J. Scott Lauritzen,[2] André Fiala,[3] Davi D. Bock,[2,4] and Gaia Tavosanis[1,5,7,*]

[1]Center for Neurodegenerative Diseases (DZNE), 53175 Bonn, Germany
[2]Janelia Research Campus, Howard Hughes Medical Institute, Ashburn, VA 20147, USA
[3]Molecular Neurobiology of Behaviour, University of Göttingen, 37077 Göttingen, Germany
[4]Department of Neurological Sciences, University of Vermont, Burlington, VT 05405, USA
[5]LIMES Institute, University of Bonn, 53115 Bonn, Germany
[6]These authors contributed equally
[7]Lead contact
*Correspondence: gaia.tavosanis@dzne.de
https://doi.org/10.1016/j.celrep.2021.108871

SUMMARY

The formation and consolidation of memories are complex phenomena involving synaptic plasticity, microcircuit reorganization, and the formation of multiple representations within distinct circuits. To gain insight into the structural aspects of memory consolidation, we focus on the calyx of the *Drosophila* mushroom body. In this essential center, essential for olfactory learning, second- and third-order neurons connect through large synaptic microglomeruli, which we dissect at the electron microscopy level. Focusing on microglomeruli that respond to a specific odor, we reveal that appetitive long-term memory results in increased numbers of precisely those functional microglomeruli responding to the conditioned odor. Hindering memory consolidation by non-coincident presentation of odor and reward, by blocking protein synthesis, or by including memory mutants suppress these structural changes, revealing their tight correlation with the process of memory consolidation. Thus, olfactory long-term memory is associated with input-specific structural modifications in a high-order center of the fly brain.

INTRODUCTION

The capacity to use past experience to guide future action is a fundamental and conserved function of the nervous system. Associative memory formation, initiated by the coincident detection of a conditioned stimulus (CS; e.g., odor) and an unconditioned stimulus (US; e.g., sugar reward), leads to a short-lived memory (STM) trace within distinct circuits (Josselyn and Tonegawa, 2020, Boto et al., 2020, Wang et al., 2008, Liu et al., 2012, Burke et al., 2012). Memories can be consolidated into long-term memories (LTMs) through processes that depend on *de novo* protein synthesis (Tully et al., 1994, Bailey et al., 1996), require structural modifications within the involved neuronal circuits, and might lead to the recruitment of additional ones (Dubnau and Chiang, 2013, Cervantes-Sandoval et al., 2013, Kitamura et al., 2017, Caroni et al., 2012, Holtmaat and Caroni, 2016, Kleim et al., 2002, Hihara et al., 2006, Bassett et al., 2011, Gu et al., 2015, Maviel et al., 2004). Compared with modulation of existing connections, the reorganization of circuits affords the unique possibility of sampling for potential new partners (Chklovskii et al., 2004, Gogolla et al., 2007, Bennett et al., 2018). Nonetheless, only few examples of rewiring associated with learning have been established thus far (Boele et al., 2013, Hihara et al., 2006, Chen et al., 2015, Poort et al., 2015, Grewe et al., 2017).

The formation and retrieval of olfactory-associative memories in *Drosophila* require the mushroom body (MB; de Belle and Heisenberg, 1994). Within the main MB input compartment, the calyx (MBC), second-order projection neurons (PNs), delivers olfactory information through cholinergic synapses to the intrinsic MB neurons, the Kenyon cells (KCs; Figure 1A). In the MBC, large, olfactory PN boutons are enwrapped by the claw-like dendrite termini of ~11 KCs on average (Butcher et al., 2012, Caron et al., 2013), thereby forming characteristic synaptic complexes, the microglomeruli (MGs; Yasuyama et al., 2002), which display functional and structural plasticity in adaptation and upon silencing (Kremer et al., 2010, Pech et al., 2015, Leiss et al., 2009). To start systematically addressing the mechanisms that support memory consolidation, we sought to investigate the properties of identifiable synaptic MGs in the MB of the adult brain of *Drosophila* after the establishment of LTMs.

Combining behavioral experiments with high-resolution microscopy and functional imaging, we demonstrate that the consolidation of appetitive olfactory memories closely correlates with an increase in the number of MGs formed by the PNs that deliver the conditioned stimulus and their postsynaptic KC partners. These structural changes result in additional, functional synaptic connections. Thus, the circuit in the calyx of the fly MB reorganizes accompanying the consolidation of associative memories.

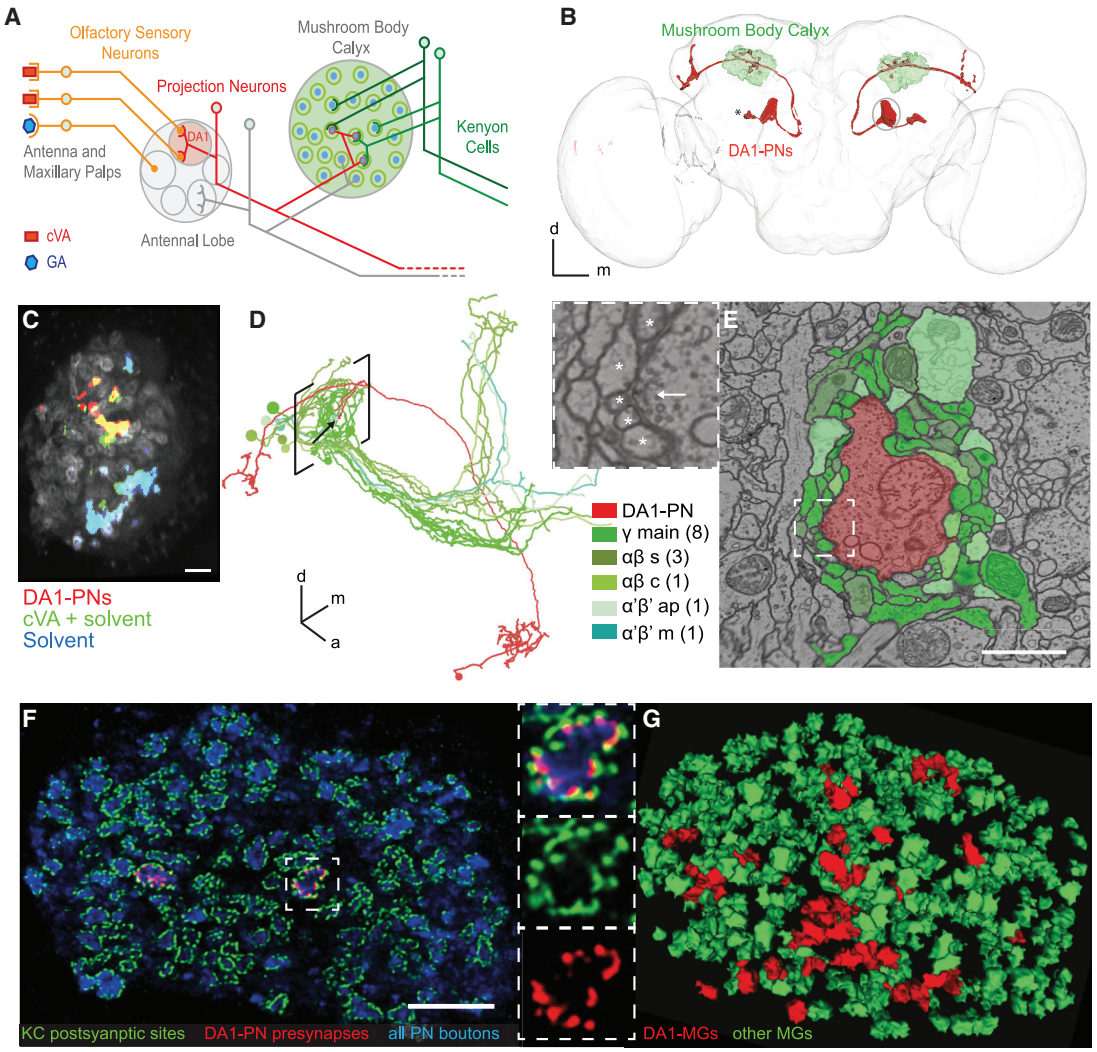

Figure 1. Identification of the synapses in the MBC responding to cVA odor stimulation

(A) Schematic representation of the olfactory circuit starting from the activation of specific olfactory sensory neurons (OSNs) by two exemplary odors, cVA and GA. In the AL, cVA-responsive OSNs converge on the DA1 glomerulus (pale red), where they synapse onto DA1-PNs (red). These deliver the cVA signal to the MBC via axon collaterals that terminate with boutons forming large synaptic complexes, the MGs (circles). Postsynaptic KCs are represented in green.

(B) Reconstruction from a full confocal serial section set of the DA1-PNs (red; *R37H08-Gal4 > UAS GAP43::Venus*); MBC (green; *MB247-Dα7::GFP*); DA1-PN cell bodies (*); brain neuropil (light gray; α-synapsin antibody).

(C) Volumetric calcium imaging of the calyx of flies carrying *MB247-Homer::GCaMP3* (gray) and in which DA1-PNs are genetically labeled (red; *R37H08-Gal4 > UAS tdTomato*). cVA-elicited postsynaptic responses (green; cVA 1:400 dissolved in 5% EtOH) are specific to DA1-PNs as revealed by the overlap between the two channels (red + green = yellow). Generic response to the solvent (cyan = overlap of the responses to cVA 1:400 dissolved in 5% EtOH, green; and to 5% EtOH only, blue). Scale bar, 10 μm.

(D) Single DA1-PN (red) and the 14 KCs (green) postsynaptic to the DA1-PN bouton indicated by the arrow. Tracings performed on the EM FAFB dataset (Zheng et al., 2018). Square brackets indicate the location of MBC. Different green shades represent different KC subtypes, as in (E). Numbers in brackets in the legend represent the number of cells.

(E) Single EM section through the MG, arrow in (D). Scale bar, 1 μm. White square is magnified in the left top panel with the arrow pointing to a T-bar of the AZ, and the asterisk (*) labels the fine dendritic postsynaptic profiles of KCs.

(F) Single plane confocal image of the MBC displaying PN boutons (blue; α-synapsin antibodies); the PSDs of KCs (green; *MB247-Dα7::GFP*) and the AZs of DA1-PN boutons only (red; *R37H08-Gal4 > UAS-brp-short^{cherry}*) identifying the cVA-responsive MGs. Scale bar, 10 μm. The MG in the white square is magnified in the right panels.

(G) Automated 3D reconstruction of a confocal stack, including the image shown in (F). The reconstruction of MGs is based on Dα7-GFP (green) (see also Figure S1), and MGs receiving presynaptic input from DA1-PNs are marked by Brp–short^{cherry} (red). All other MGs are in green.

Full genotypes used and statistics for Figures 1, 2, 3, and 4 are included in Table S2.

RESULTS

Identifiable synaptic microglomeruli in the calyx respond to cVA

To reveal potential changes in synapse organization linked to memory consolidation, we first developed a setup allowing us to identify the individual synapses of olfactory PNs that deliver a conditioned odor to the MB. The pheromone and odorant 11-*cis*-vaccenylacetate (cVA) specifically activates PNs that project their dendrites to the DA1 glomerulus in the antennal lobe (AL) (Datta et al., 2008, Kurtovic et al., 2007, Schlief and Wilson, 2007). The DA1 glomerulus is mostly excluded from complex processing of sensory information in the AL (Lebreton et al., 2014, Lebreton et al., 2015), suggesting that, by genetically marking the DA1 PNs, we could identify the individual boutons in the MBC that deliver the olfactory response to cVA. We tested this by recording, with volumetric calcium imaging, the response to odor stimulation in the MBC of animals expressing a genetically encoded calcium indicator tethered at the KC postsynapses (Pech et al., 2015) in combination with a presynaptic fluorescent tag (*UAS-tdTomato*) expressed in DA1 PNs only (Figure 1C). Regions of interest (ROIs) containing fluorescently labeled DA1-MGs showed a postsynaptic response specifically tuned to cVA stimulation (84% ± 8% of the fluorescently labeled DA1-MGs responded to cVA and not to the solvent alone, 9% ± 7% did not respond to cVA or the solvent, and 7% ± 5% responded to both. Data are expressed as means ± SD; n = 7; Figure 1C).

Therefore, by selecting the combination of the cVA odorant and the DA1 subset of PNs, we established a system in which we can track a fly's neuronal response toward a specific odor on the level of individual synaptic complexes in the MBC (Figures 1A–1C).

To gain insight into the complexity of the MG microcircuit formed by a single DA1-PN bouton, we took advantage of the availability of an adult whole-brain electron microscopy (EM) volume (Zheng et al., 2018). With this dataset, we reconstructed a complete MG connectome by tracing neurites from every pre- and postsynaptic contact of a DA1-PN bouton until the corresponding neuron's identity was anatomically determinable (Figures 1D and 1E; Table S1). This particular DA1-PN bouton made 33 excitatory cholinergic contacts, all polyadic and identifiable by the presence of a T-bar and a synaptic cleft (Figure 1E, inset), apposed to 277 postsynaptic profiles. Most profiles (248) postsynaptic to the bouton originated from 14 KCs of five different subtypes: γmain (8), αβs (3), αβc (1), α′β′ap (1), and α′β′m (1) (Aso et al., 2014). γMain profiles were the most abundant in this particular bouton, although DA1-PN boutons are located within a region of the MBC predominantly occupied by αβs KCs (Lin et al., 2007). Each KC contacted the bouton with a single claw receiving eight to 25 presynaptic inputs from the PN bouton, in line with previous estimates (Butcher et al., 2012, Leiss et al., 2009). Within the MG, the bouton received presynaptic input from four cells: two additional γmain KCs forming divergent triads that included a KC, the PN bouton, and the anterior paired lateral neuron (Liu and Davis, 2009); APL itself, and one of the two MB calyx 1 neurons (MB-C1) (Table S1). Taken together, a single MG represents a highly complex microcircuit, involving many neurons (19 in this example) of different types (here, eight).

Structural changes in calycal MGs upon memory consolidation

To investigate whether such a complex structure undergoes plastic changes, we designed a setup to observe and measure the properties of identifiable MGs after olfactory conditioning.

In confocal images, we highlighted cVA-responsive MGs in the MBC by expressing the presynaptic active zone (AZ) marker Brp-short^{cherry} in DA1-PNs only (Schmid et al., 2008, Kremer et al., 2010). The postsynaptic densities (PSDs) of KC dendrites were decorated by cell-type-specific expression of the GFP-tagged Dα7 subunit of the acetylcholine receptor (Kremer et al., 2010). We developed a software-based automated three-dimensional (3D)-reconstruction tool to identify the MGs exploiting the *MB247-Dα7::GFP* signal and classified them as DA1-PN-positive if they additionally displayed Brp-short^{cherry} co-labeling (DA1-MG; Figures 1G and S1). Further, we established a standard appetitive-associative conditioning paradigm using cVA or geranyl acetate (GA) as CS in STM or LTM paradigms (Figures 2A and S2A–S2C; see STAR Methods) and applied it to flies expressing the reporters described above (Figures 2B, 2F, and 2J). Alternatively, we mock-trained the flies by presenting odors and sugar reward separately to avoid the formation of appetitive association (Figures 2A, 2B, 2F, and 2J; Tempel et al., 1983). GA was chosen because it activates a separate and non-overlapping set of PNs in comparison to cVA (Bhandawat et al., 2007), and 5% EtOH was added to both odors to provide a food-related context to the starved flies (Lebreton et al., 2015, Pohl et al., 2012), which was essential to elicit STM (Figure S2B). To assess whether MGs formed by DA1-PN boutons (DA1-MGs) underwent morphological modifications after learning, we prepared for confocal imaging female fly brains dissected at 1 min (STM) or at 24 h (LTM) after training. After STM establishment (Figure 2B), the total number, MG volume, and lumen volume of DA1-MGs was unchanged in cVA-conditioned (cVA CS$^+$) flies compared with the GA-conditioned (GA CS$^+$) or mock control groups (average MG numbers: mock 28.91; GA CS$^+$ 30.40; cVA CS$^+$ 28.76; n = 10–17; Figures 2C–2E). However, in the LTM paradigm (Figure 2F), the DA1-MGs total volume and lumen volume were decreased in cVA CS$^+$ flies compared with GA CS$^+$ or mock-control flies (Figures 2G and 2H). In addition, the total number of DA1-MGs was increased (average MG numbers: mock 27.31; GA CS$^+$ 27.47; cVA CS$^+$ 32.06; n = 18-32; Figure 2I). Thus, LTM, but not STM, was accompanied by an input-specific structural reorganization of the MBC circuit, including an increase in MG number. These changes were specific to the conditioned odor because they did not appear in the DA1-MGs when the conditioned odor was GA. These data suggest that the neurons delivering the CS form new boutons, which are smaller and are enveloped by KC claws.

Olfactory associative learning relies on the function of the Ca^{2+}/CaM-dependent adenylyl cyclase Rutabaga (Tempel et al., 1983, Levin et al., 1992, Thum et al., 2007), and a defining trait of LTM is its dependence on protein synthesis (Lagasse et al., 2009, Tully et al., 1994, Davis, 2011). Indeed, a mutation in the *rutabaga* gene (*rut*^{2080}(Han et al., 1992) or feeding flies with the protein synthesis inhibitor cycloheximide (CHX) immediately after training abolished LTM (Figures 2J and S2D). Importantly, loss of *rut* function or CHX feeding also suppressed the

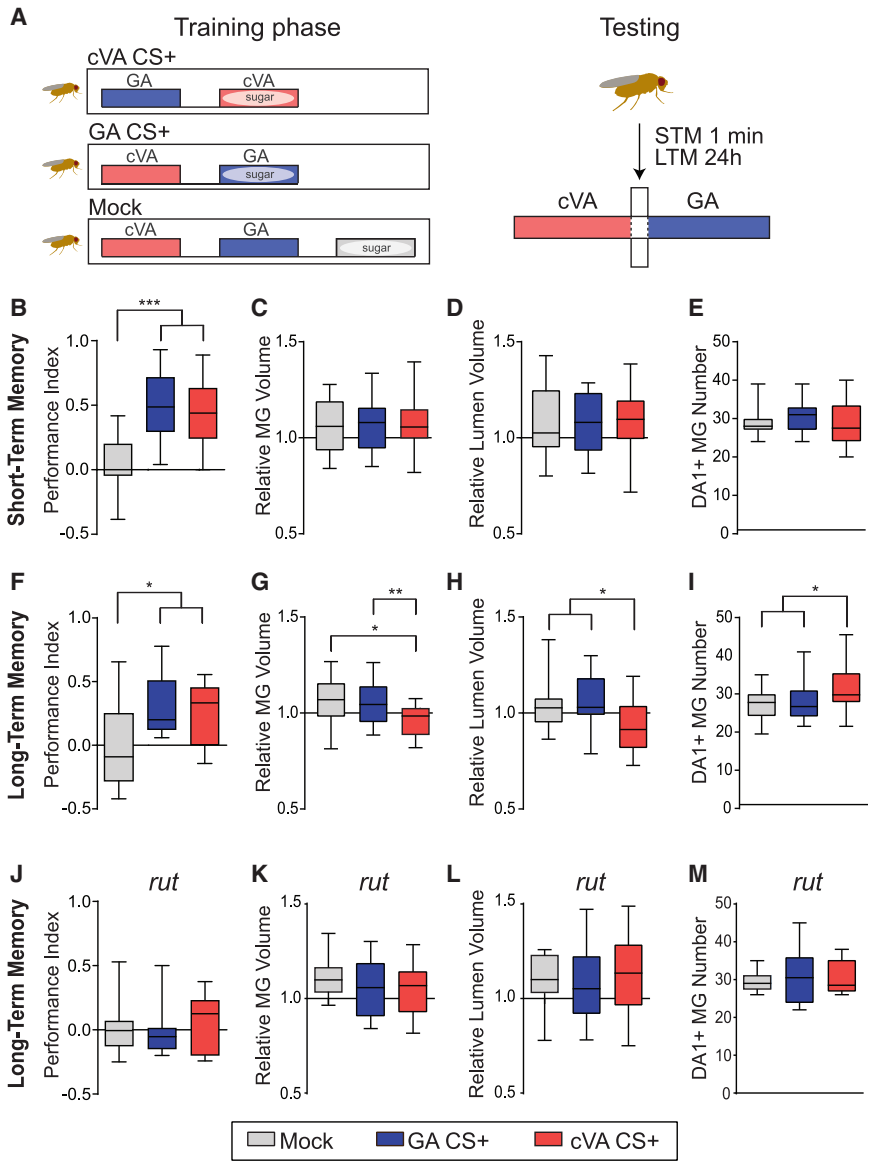

Figure 2. Microglomeruli undergo structural changes upon appetitive long-term memory formation

(A) Schematic illustration of the appetitive-conditioning paradigm. For training, the conditioned odor cVA (red box) or GA (blue box) is paired with sugar. In STM experiments, flies are trained for 2 min with a 2 min interval between CS^+ and CS^- presentation and tested 1 min after training. In LTM experiments, flies are trained for 5 min + 5 min with a 2-min stimulus interval and are tested 24 h after training. In the mock control, the two odors and the sugar reward are presented in a temporally spaced sequence with a 2-min inter-stimulus pause.

(B, F, and J) Performance indices of flies *R37H08-Gal4/MB247-DαGFP, UAS-brp-short^{cherry}* in the STM (B), ***$p < 0.001$, $n = 19–25$; or in the LTM paradigm (F), *$p < 0.05$, $n = 14–19$; and the performance index of *rut* mutant flies in LTM (J), $p > 0.05$, $n = 17–18$. Performance index values of the mock control group (gray) were compared with groups trained with GA CS^+ (blue) or cVA CS^+ (red). Multiple comparisons are tested throughout this study with one-way ANOVA with Bonferroni correction. Significance level is set at $p < 0.05$. *$p < 0.05$, ****$p < 0.0001$.

(C, G, and K) The MG volume comprises the volume contained within a ring of *MB247-Dα7::GFP* PSDs and the volume of the *MB247-Dα7::GFP* PSDs .

(D, H, and L) The MG lumen is the volume contained within a ring of *MB247-Dα7::GFP* PSDs (see Figure S1D). In STM, the relative volume (ratio of the average DA1-MG/non-DA1-MG per animal) of DA1- MGs (C) and of their lumen (D) is not different between groups ($p > 0.05$, $n = 15–20$). In LTM, the relative MG volume (G) and lumen volume (H) of DA1-MGs in flies trained with cVA CS^+ are smaller than in flies from the mock control group or in flies trained with GA CS^+ (*$p < 0.05$, **$p < 0.01$, $n = 19–25$).

(E, I, and M) Number of DA1-PN-positive MGs is unaffected in STM (E) ($p > 0.05$, $n = 18–24$). In LTM, number of DA1-PN-positive MGs in cVA CS^+ trained flies is greater compared with flies of the mock control or GA CS^+ group (I) (*$p < 0.05$, $n = 18–24$). The structural modifications of DA1- MGs in cVA CS^+ trained flies after the appetitive LTM protocol, were suppressed in *rut* mutants (K)–(M) ($p > 0.05$, $n = 13–21$). In all boxplots, the edges of the boxes are the first and third quartiles, thick lines mark the medians, and whiskers represent data range.

structural changes in the DA1-MGs, supporting the correlation between LTM formation and structural changes in the circuit (Figures 2K–2M and S2E–S2G).

The increase in DA1-PN-positive MG number after LTM formation with cVA CS^+ suggests that new boutons might be formed during consolidation. To gain insight into the cellular fundamentals of these modifications, we expressed the membrane-tagged fluorescent protein *UAS-GAP43::Venus* in DA1-PN axons, together with *UAS-brp-short^{cherry}*, and highlighted the postsynaptic densities on KC dendrites using *MB247-Dα7::GFP* (Figures 3A–3D). Serial optical sections of the MBCs of these flies trained with cVA CS^+, with GA CS^+, or in the mock paradigm (Figure S2H) were used to generate 3D reconstructions that were then aligned to a reference brain (JFRC2; Jenett et al., 2012). The DA1-PN axons were then traced in the aligned high-resolution scans of the MBC (Figure 3E). The DA1-PN boutons were highly clustered in the dorsal-posterior part of the calyx (Clark and Evans, 1954), supporting the view that the localization of DA1-PN boutons within the MBC is not entirely random (Figure 3F; Jefferis et al., 2007). The total length of DA1-PN collaterals measured from the point at which they leave the inner antennocerebral tract (iACT) was increased in flies that had formed LTMs after cVA CS^+ training compared with mock-control flies (Figure 3G). In addition, the total volume within the MBC containing DA1-PN-positive boutons was increased in flies that had formed cVA CS^+ LTMs (Figure 3H). These observations suggest that during

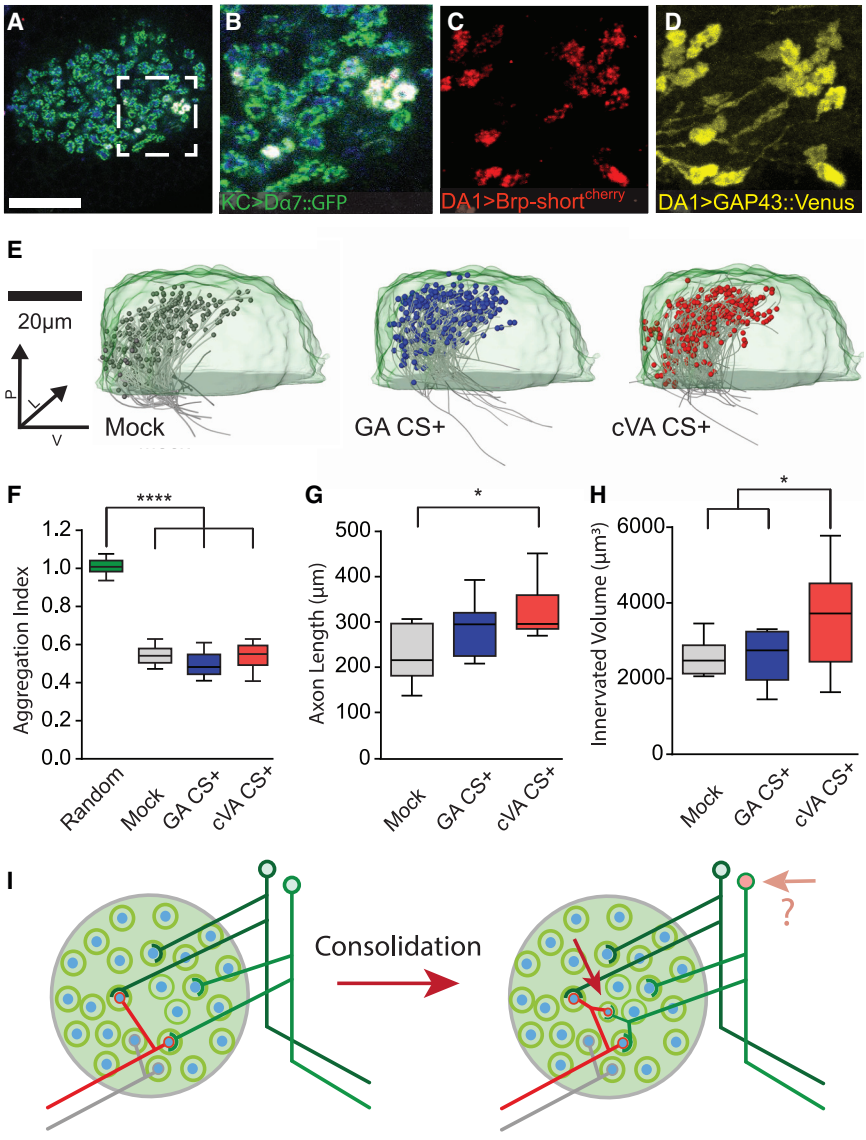

Figure 3. Modifications of axon collaterals and wiring properties of projection neurons within the mushroom body calyx after long-term memory formation

(A) Single optical section of the MBC of flies expressing Dα7GFP (green) in the KCs and Brp-short^{cherry} (red) plus GAP43-Venus (yellow) in DA1-PNs (*R37H08-Gal4*); PN boutons (blue; anti-Synapsin antibodies). Scale bar, 20 µm.

(B–D) Magnification of the white square in (A) displaying its merge (B) or a maximum-intensity projection of Brp-short^{cherry} (C) or of GAP43-Venus (D) signals.

(E) Medial view of registered PN axons (gray) with traced boutons (gray, blue, red spheres) within a standard calyx (light green). The registered PN traces are of mock (gray), GA CS$^+$ (blue) or cVA CS$^+$ (red) trained groups. n = 10 for each group.

(F) Boutons are highly clustered, independent of the treatment (Clark and Evans aggregation index compared with a hypothetical random distribution; ****$p < 0.0001$, n = 10).

(G) Total collateral axons length of mock control, GA CS$^+$ or cVA CS$^+$ flies. (*$p < 0.05$, n = 10).

(H) The convex hull volume containing all DA1-boutons in the MBC per condition is increased in cVA CS$^+$ flies compared with the mock control and GA CS$^+$ group (*$p < 0.05$, n = 10).

(I) We suggest that the increased number of MGs after consolidation is due to the formation of additional boutons responding to cVA. The additional boutons form full MGs, as postsynaptic profiles of KCs surround them. It is unclear whether this reorganization might lead to the recruitment of additional responding KCs (see Discussion). In all boxplots, the edges of the boxes are the first and third quartiles, thick lines mark the medians, and whiskers represent data range.

consolidation, additional boutons are created by local growth at existing DA1-PN collaterals (Figure 3I).

Altered functional response in calycal microglomeruli upon memory consolidation

To address whether the observed structural changes within the MGs after LTM effect on the functional representation of the CS in the MBC, we analyzed calcium dynamics in KC dendrites. For that, we used flies carrying *MB247-homer::GCaMP3* (Pech et al., 2015), in combination with volumetric calcium imaging (Figure 4A). We used this simple genotype to guarantee that flies performed well in LTM experiments (Figure S2I). We measured calcium response in the entire MBC volume during a single odor application (5 s odor stimulation) of either cVA (1:400 in 5% EtOH) or EtOH alone (5%). To identify areas with increased calcium dynamics during odor stimulation, we overlaid a grid consisting of 5 × 5-µm^2 ROIs over each optical section of the volumetric time series. Based on the grid segmentation, we then calculated the average ΔF/F% for each ROI in the MBC. ROIs were classified as odor responsive if the measured calcium response exceeded a set threshold (ΔF/F% > 3 × SD; see STAR Methods) during the first 2 s of stimulation (Figures 4B, 4C, S3A, and S3B). The response pattern elicited specifically by cVA was defined after subtraction of the EtOH response (Figures 4C, S3C, and S3D; see also Figure 1C and STAR Methods). After appetitive LTM formation, the percentage of cVA-responsive ROIs was increased in cVA CS$^+$ flies compared with the mock control (Figure 4D; n = 7, $p < 0.05$), suggesting that the additional DA1-PN boutons are functionally connected to their postsynaptic KC counterparts and are capable of initiating a response in the postsynaptic KCs. Linear regression analysis of the fluorescence change over time during odor stimulation showed a steeper drop of the linear fit in cVA CS$^+$ flies (R^2 = 0.6429) toward baseline compared with flies of the mock control group (R^2 = 0.1124) (Figures 4E and 4F). In addition, the response toward the odor was more variable in mock-trained flies compared with the cVA CS$^+$ flies (Figure S3F). Initially (0–4 s after

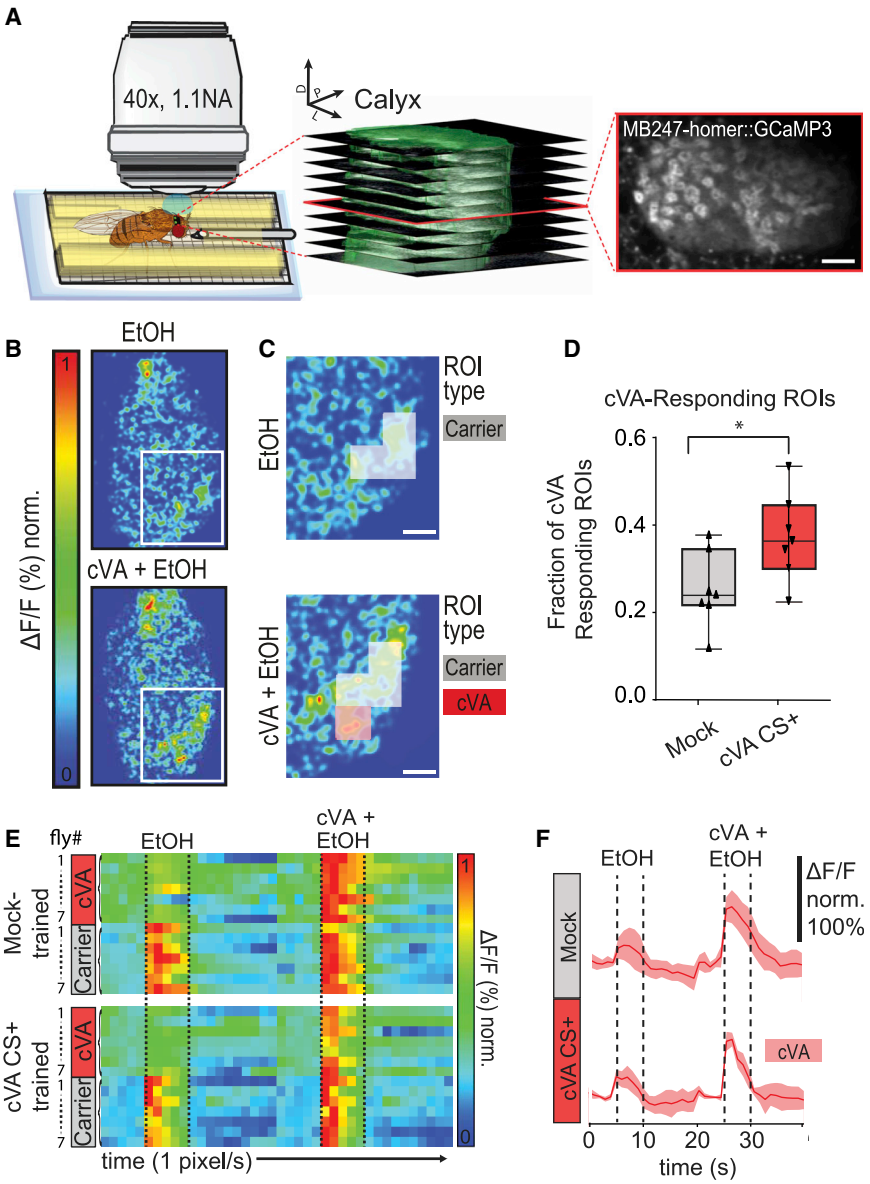

Figure 4. Functional plasticity in the mushroom body calyx associated with long-term memory

(A) Two-photon *in vivo* imaging setup. Schematic of a fly placed on a custom-made holder under a two-photon microscope equipped with a ×40 1.1 NA water-immersion objective. The odor was delivered for 5 s with a moisturized, constant air stream through a 1.2-mm cannula. (Center) z series of the entire MBC volume of flies expressing post-synapse-tagged Homer-GCaMP3 imaged during odor application at 1 Hz (10 optical sections per volume, 4-μm step size). (Right) A single slice of the image stack shown in the middle panel. Scale bar, 10 μm.

(B) Representative optical section from a volumetric time series showing false-colored response of KC dendrites to 5-s exposure to EtOH (top) or cVA + EtOH (bottom).

(C) Magnification of the white square area in (B). 5 × 5-μm^2 ROIs were classified as cVA-responsive (red) if they were only active during cVA + EtOH application but did not respond to EtOH alone. ROIs that responded to both conditions were classified as carriers. Scale bar, 5 μm.

(D) The fraction of cVA responsive ROIs increased after LTM acquisition compared with that of the mock control (boxplot represents first and third quartiles, thick lines mark the medians, and whiskers represent data range. *$p < 0.05$, $n = 7$).

(E) Dynamics of ΔF/F% changes over time in KCs of *MB247-homer::GCaMP3* flies after mock training (top) or LTM acquisition (bottom). Each row of the heatmap represents average responses per animal of all cVA-responsive ROIs (red) or of all carrier EtOH-responsive ROIs (gray) within one MBC over time. Each column represents 1 s. Flies are first exposed to the EtOH (5 s) and then to cVA + EtOH (5 s), as indicated by the dashed lines.

(F) Plot of average calcium dynamics over time of cVA-responsive ROIs during 5-s stimulation with EtOH or with cVA in EtOH (dashed lines) in mock-trained (top) or cVA CS^+ (bottom) flies ($n = 7$). Data are represented as means ± SD.

start of stimulation), the total response toward cVA stimulation was indistinguishable between mock control and cVA CS^+ group. However, at subsequent time points (4–7 s after start of stimulation) responses were significantly lower in KC dendrites of the cVA CS^+ group compared with the mock control, showing a faster calcium decay toward the trained odor in CS^+ flies ($n = 7$, $p < 0.05$) (Figure S3G). Together, these data indicate a temporal sharpening of the odor response.

DISCUSSION

We report input-specific reorganization of the adult MBC circuit associated with the formation of long-term, appetitive memory. By visualizing presynaptic markers in PNs and the KC postsynaptic densities, we uncover an increase in the number of PN boutons and, at the same time, reveal that these boutons are enveloped by KC postsynaptic profiles, suggesting that new MGs are formed during memory consolidation. These findings are particularly remarkable, given the high degree of complexity of the MG microcircuits revealed by our EM reconstruction and including the dendrite claws of multiple KCs of distinct subtypes. The cellular mechanisms leading to the increased number of odor-specific complex MGs remain to be clarified, but they will require a tight coordination between pre- and postsynaptic partners. In this context, mutations in synaptic proteins or in proteins mediating cell-cell interactions, which specifically block LTM, will be of great interest (Silva et al., 2020, Gouzi et al., 2018). We suggest that remodeling could be driven by intrinsic reactivation of KCs during the consolidation phase (Ichinose et al., 2015, Cognigni et al., 2018) or by modulatory inputs into the calyx (Mao and

Davis, 2009, Chen et al., 2012, Aso et al., 2014, Busch et al., 2009, Boto et al., 2019). In either case, we expect a complex pattern of activation, which might be difficult to reproduce in artificial settings (Kremer et al., 2010, Warth Pérez Arias et al., 2020). Although our present observations are limited for technical reasons to the specific case of cVA, the overall density of PN boutons in the MBC increases after appetitive long-term conditioning in honeybees, as well as in leaf-cutting ants after avoidance learning (Hourcade et al., 2010, Falibene et al., 2015). Based on that and given that the olfactory pathway of cVA is not distinguishable from that of other odors, we thus suggest that our findings might be generalizable. In comparison with those systems, however, we use genetic and functional identification of PN subsets to reveal that the structural modifications are specific and limited to the PNs conveying the conditioned odor. Importantly, our *in vivo* functional imaging data support the view that the circuit reorganization leads to additional functional MGs responding to the conditioned odor. In addition, they demonstrate a specific change in functional response in the KC dendrites toward the trained odor because the calcium levels drop faster toward baseline after appetitive associative conditioning. The faster decay kinetics and more skewed response toward the onset of the stimulus could contribute to a more-efficient temporal summation of responses or refine the KC response and might be related to inhibitory modifications (Gupta and Stopfer, 2014, Haenicke et al., 2018). An important open question is the effect of the increased number of responding MGs on the pattern of KC activation. KCs respond sparsely to odor input and require the coincident activation of multiples of their claws to produce an action potential (Gruntman and Turner, 2013). Our data might underlie the addition of connections between the active PNs and a set of already-responding KCs, leading to facilitated response to the conditioned odor without changing the set of responding KCs. A recent publication, however, suggests an exciting alternative view. After aversive LTM establishment, the number of KCs responding to the conditioned odor is increased (Delestro et al., 2020). If we hypothesize that appetitive conditioning leads to a similar outcome, our data could provide anatomical and functional support to these findings. The pattern of KC response could, thus, be modulated by experience in adulthood and might represent a rich signifier of sensory stimulus and context. Reconstruction of an MG from EM serial sections derived from FAFB dataset (Zheng et al., 2018). Video S1 shows a DA1-PN bouton (red) and all profiles that are directly pre- or postsynaptic to it. The DA1-PN bouton is surrounded by the claws of 14 KCs of five subtypes (different green shades according to Figures 1D and 1E). Three additional neurons contribute to this MG: APL (blue), which is pre- and postsynaptic to the PN bouton, and both MB-C1 neurons (yellow). Finally, two γmain KCs (dark green) form presynaptic connections with the bouton. See also Table S1. All genotypes and statistical tests (including p values) used throughout the document, are ordered by appearance.

STAR★METHODS

Detailed methods are provided in the online version of this paper and include the following:

SUPPLEMENTAL INFORMATION

Supplemental information can be found online at https://doi.org/10.1016/j.celrep.2021.108871.

ACKNOWLEDGMENTS

We thank LMF and IDAF sections at DZNE and A. Mueller, R. Kerpen, and J. C. Vijayakumar for technical assistance. We are grateful to C.B. Fisher, S.A. Calle-Schuler, N. Sharifi, B. Gorko, L. Kmecova, I.J. Ali, N. Masoodpanah, J. Hsu, and F. Li in the D.D.B. laboratory for their support in tracing evaluation. We thank Y. Aso, HHMI Janelia, the Kyoto Drosophila Genetic Resource Center, and the Bloomington Stock Center for fly lines and FlyBase. We are grateful for their assistance to the DZNE IDAF in the establishment of the cluster analysis, S. Dipt with initial calcium imaging experiments, and R. Court for providing the brain aligner and support. We thank S. Sachse, D. Isbrandt, T. Hige, S. Remy, M. Nawrot, O. Barnstedt, the members of the Tavosanis lab for discussion and/or critical reading of the manuscript, and B. Schaffran for help with video editing. L.B. acknowledges support by the Bonn International Graduate School of Neuroscience. This work was supported by the DFG FOR 2705 to G.T.

AUTHOR CONTRIBUTIONS

L.B. and G.T. conceived the project and designed the experiments. L.B., P.R., and L.P. constructed fly strains, performed the behavioral experiments, and produced and analyzed the anatomical data. J.S.L. and D.D.B. established the set of EM data, and P.R. performed the tracings presented here. Scripts and routines for the analysis were established by L.B. and L.P. Functional imaging experiments were designed and performed by L.B and L.P. with support from A.F. The manuscript was written by G.T., L.B., P.R., and L.P.

DECLARATION OF INTERESTS

The authors declare no competing interests.

Received: August 26, 2020
Revised: January 7, 2021
Accepted: February 24, 2021
Published: March 16, 2021

REFERENCES

Aso, Y., Hattori, D., Yu, Y., Johnston, R.M., Iyer, N.A., Ngo, T.T., Dionne, H., Abbott, L.F., Axel, R., Tanimoto, H., and Rubin, G.M. (2014). The neuronal

architecture of the mushroom body provides a logic for associative learning. eLife *3*, e04577.

Bailey, C.H., Bartsch, D., and Kandel, E.R. (1996). Toward a molecular definition of long-term memory storage. Proc. Natl. Acad. Sci. USA *93*, 13445–13452.

Bassett, D.S., Wymbs, N.F., Porter, M.A., Mucha, P.J., Carlson, J.M., and Grafton, S.T. (2011). Dynamic reconfiguration of human brain networks during learning. Proc. Natl. Acad. Sci. USA *108*, 7641–7646.

Bennett, S.H., Kirby, A.J., and Finnerty, G.T. (2018). Rewiring the connectome: evidence and effects. Neurosci. Biobehav. Rev. *88*, 51–62.

Bhandawat, V., Olsen, S.R., Gouwens, N.W., Schlief, M.L., and Wilson, R.I. (2007). Sensory processing in the Drosophila antennal lobe increases reliability and separability of ensemble odor representations. Nat. Neurosci. *10*, 1474–1482.

Boele, H.J., Koekkoek, S.K., De Zeeuw, C.I., and Ruigrok, T.J. (2013). Axonal sprouting and formation of terminals in the adult cerebellum during associative motor learning. J. Neurosci. *33*, 17897–17907.

Boto, T., Stahl, A., Zhang, X., Louis, T., and Tomchik, S.M. (2019). Independent contributions of discrete dopaminergic circuits to cellular plasticity, memory strength, and valence in *Drosophila*. Cell Rep. *27*, 2014–2021.e2.

Boto, T., Stahl, A., and Tomchik, S.M. (2020). Cellular and circuit mechanisms of olfactory associative learning in *Drosophila*. J. Neurogenet. *34*, 36–46.

Burke, C.J., Huetteroth, W., Owald, D., Perisse, E., Krashes, M.J., Das, G., Gohl, D., Silies, M., Certel, S., and Waddell, S. (2012). Layered reward signalling through octopamine and dopamine in *Drosophila*. Nature *492*, 433–437.

Busch, S., Selcho, M., Ito, K., and Tanimoto, H. (2009). A map of octopaminergic neurons in the *Drosophila* brain. J. Comp. Neurol. *513*, 643–667.

Butcher, N.J., Friedrich, A.B., Lu, Z., Tanimoto, H., and Meinertzhagen, I.A. (2012). Different classes of input and output neurons reveal new features in microglomeruli of the adult *Drosophila* mushroom body calyx. J. Comp. Neurol. *520*, 2185–2201.

Cardona, A., Saalfeld, S., Schindelin, J., Arganda-Carreras, I., Preibisch, S., Longair, M., Tomancak, P., Hartenstein, V., and Douglas, R.J. (2012). TrakEM2 software for neural circuit reconstruction. PLoS ONE *7*, e38011.

Caron, S.J., Ruta, V., Abbott, L.F., and Axel, R. (2013). Random convergence of olfactory inputs in the *Drosophila* mushroom body. Nature *497*, 113–117.

Caroni, P., Donato, F., and Muller, D. (2012). Structural plasticity upon learning: regulation and functions. Nat. Rev. Neurosci. *13*, 478–490.

Cervantes-Sandoval, I., Martin-Peña, A., Berry, J.A., and Davis, R.L. (2013). System-like consolidation of olfactory memories in *Drosophila*. J. Neurosci. *33*, 9846–9854.

Chen, C.C., Wu, J.K., Lin, H.W., Pai, T.P., Fu, T.F., Wu, C.L., Tully, T., and Chiang, A.S. (2012). Visualizing long-term memory formation in two neurons of the *Drosophila* brain. Science *335*, 678–685.

Chen, J.L., Margolis, D.J., Stankov, A., Sumanovski, L.T., Schneider, B.L., and Helmchen, F. (2015). Pathway-specific reorganization of projection neurons in somatosensory cortex during learning. Nat. Neurosci. *18*, 1101–1108.

Chklovskii, D.B., Mel, B.W., and Svoboda, K. (2004). Cortical rewiring and information storage. Nature *431*, 782–788.

Clark, P.J., and Evans, F.C. (1954). Distance to nearest neighbour as a measure of spatial relationships in populations. Ecology *35*, 445–453.

Cognigni, P., Felsenberg, J., and Waddell, S. (2018). Do the right thing: neural network mechanisms of memory formation, expression and update in *Drosophila*. Curr. Opin. Neurobiol. *49*, 51–58.

Costa, M., Manton, J.D., Ostrovsky, A.D., Prohaska, S., and Jefferis, G.S. (2016). NBLAST: rapid, sensitive comparison of neuronal structure and construction of neuron family databases. Neuron *91*, 293–311.

Cuntz, H., Forstner, F., Borst, A., and Häusser, M. (2010). One rule to grow them all: a general theory of neuronal branching and its practical application. PLoS Comput. Biol. *6*, e1000877.

Datta, S.R., Vasconcelos, M.L., Ruta, V., Luo, S., Wong, A., Demir, E., Flores, J., Balonze, K., Dickson, B.J., and Axel, R. (2008). The *Drosophila* pheromone cVA activates a sexually dimorphic neural circuit. Nature *452*, 473–477.

Davis, R.L. (2011). Traces of *Drosophila* memory. Neuron *70*, 8–19.

de Belle, J.S., and Heisenberg, M. (1994). Associative odor learning in *Drosophila* abolished by chemical ablation of mushroom bodies. Science *263*, 692–695.

Delestro, F., Scheunemann, L., Pedrazzani, M., Tchenio, P., Preat, T., and Genovesio, A. (2020). In vivo large-scale analysis of *Drosophila* neuronal calcium traces by automated tracking of single somata. Sci. Rep. *10*, 7153.

Dubnau, J., and Chiang, A.S. (2013). Systems memory consolidation in *Drosophila*. Curr. Opin. Neurobiol. *23*, 84–91.

Falibene, A., Roces, F., and Rössler, W. (2015). Long-term avoidance memory formation is associated with a transient increase in mushroom body synaptic complexes in leaf-cutting ants. Front. Behav. Neurosci. *9*, 84.

Gogolla, N., Galimberti, I., and Caroni, P. (2007). Structural plasticity of axon terminals in the adult. Curr. Opin. Neurobiol. *17*, 516–524.

Gouzi, J.Y., Bouraimi, M., Roussou, I.G., Moressis, A., and Skoulakis, E.M.C. (2018). The *Drosophila* receptor tyrosine kinase Alk constrains long-term memory formation. J. Neurosci. *38*, 7701–7712.

Grabe, V., Strutz, A., Baschwitz, A., Hansson, B.S., and Sachse, S. (2015). Digital in vivo 3D atlas of the antennal lobe of *Drosophila* melanogaster. J. Comp. Neurol. *523*, 530–544.

Grewe, B.F., Gründemann, J., Kitch, L.J., Lecoq, J.A., Parker, J.G., Marshall, J.D., Larkin, M.C., Jercog, P.E., Grenier, F., Li, J.Z., et al. (2017). Neural ensemble dynamics underlying a long-term associative memory. Nature *543*, 670–675.

Gruntman, E., and Turner, G.C. (2013). Integration of the olfactory code across dendritic claws of single mushroom body neurons. Nat. Neurosci. *16*, 1821–1829.

Gu, S., Pasqualetti, F., Cieslak, M., Telesford, Q.K., Yu, A.B., Kahn, A.E., Medaglia, J.D., Vettel, J.M., Miller, M.B., Grafton, S.T., and Bassett, D.S. (2015). Controllability of structural brain networks. Nat. Commun. *6*, 8414.

Gupta, N., and Stopfer, M. (2014). A temporal channel for information in sparse sensory coding. Curr. Biol. *24*, 2247–2256.

Haenicke, J., Yamagata, N., Zwaka, H., Nawrot, M., and Menzel, R. (2018). Neural correlates of odor learning in the presynaptic microglomerular circuitry in the honeybee mushroom body calyx. eNeuro *5*, eneuro.0128-18.2018.

Han, P.L., Levin, L.R., Reed, R.R., and Davis, R.L. (1992). Preferential expression of the *Drosophila* rutabaga gene in mushroom bodies, neural centers for learning in insects. Neuron *9*, 619–627.

Hihara, S., Notoya, T., Tanaka, M., Ichinose, S., Ojima, H., Obayashi, S., Fujii, N., and Iriki, A. (2006). Extension of corticocortical afferents into the anterior bank of the intraparietal sulcus by tool-use training in adult monkeys. Neuropsychologia *44*, 2636–2646.

Holtmaat, A., and Caroni, P. (2016). Functional and structural underpinnings of neuronal assembly formation in learning. Nat. Neurosci. *19*, 1553–1562.

Hourcade, B., Muenz, T.S., Sandoz, J.C., Rössler, W., and Devaud, J.M. (2010). Long-term memory leads to synaptic reorganization in the mushroom bodies: a memory trace in the insect brain? J. Neurosci. *30*, 6461–6465.

Ichinose, T., Aso, Y., Yamagata, N., Abe, A., Rubin, G.M., and Tanimoto, H. (2015). Reward signal in a recurrent circuit drives appetitive long-term memory formation. eLife *4*, e10719.

Jefferis, G.S., Potter, C.J., Chan, A.M., Marin, E.C., Rohlfing, T., Maurer, C.R., Jr., and Luo, L. (2007). Comprehensive maps of *Drosophila* higher olfactory centers: spatially segregated fruit and pheromone representation. Cell *128*, 1187–1203.

Jenett, A., Rubin, G.M., Ngo, T.T., Shepherd, D., Murphy, C., Dionne, H., Pfeiffer, B.D., Cavallaro, A., Hall, D., Jeter, J., et al. (2012). A GAL4-driver line resource for *Drosophila* neurobiology. Cell Rep. *2*, 991–1001.

Josselyn, S.A., and Tonegawa, S. (2020). Memory engrams: Recalling the past and imagining the future. Science *367*, eaaw4325.

Kitamura, T., Ogawa, S.K., Roy, D.S., Okuyama, T., Morrissey, M.D., Smith, L.M., Redondo, R.L., and Tonegawa, S. (2017). Engrams and circuits crucial for systems consolidation of a memory. Science *356*, 73–78.

Kleim, J.A., Freeman, J.H., Jr., Bruneau, R., Nolan, B.C., Cooper, N.R., Zook, A., and Walters, D. (2002). Synapse formation is associated with memory storage in the cerebellum. Proc. Natl. Acad. Sci. USA *99*, 13228–13231.

Kremer, M.C., Christiansen, F., Leiss, F., Paehler, M., Knapek, S., Andlauer, T.F., Förstner, F., Kloppenburg, P., Sigrist, S.J., and Tavosanis, G. (2010). Structural long-term changes at mushroom body input synapses. Curr. Biol. *20*, 1938–1944.

Kurtovic, A., Widmer, A., and Dickson, B.J. (2007). A single class of olfactory neurons mediates behavioural responses to a *Drosophila* sex pheromone. Nature *446*, 542–546.

Lagasse, F., Devaud, J.M., and Mery, F. (2009). A switch from cycloheximide-resistant consolidated memory to cycloheximide-sensitive reconsolidation and extinction in *Drosophila*. J. Neurosci. *29*, 2225–2230.

Lebreton, S., Grabe, V., Omondi, A.B., Ignell, R., Becher, P.G., Hansson, B.S., Sachse, S., and Witzgall, P. (2014). Love makes smell blind: mating suppresses pheromone attraction in *Drosophila* females via Or65a olfactory neurons. Sci. Rep. *4*, 7119.

Lebreton, S., Trona, F., Borrero-Echeverry, F., Bilz, F., Grabe, V., Becher, P.G., Carlsson, M.A., Nässel, D.R., Hansson, B.S., Sachse, S., and Witzgall, P. (2015). Feeding regulates sex pheromone attraction and courtship in *Drosophila* females. Sci. Rep. *5*, 13132.

Leiss, F., Groh, C., Butcher, N.J., Meinertzhagen, I.A., and Tavosanis, G. (2009). Synaptic organization in the adult *Drosophila* mushroom body calyx. J. Comp. Neurol. *517*, 808–824.

Levin, L.R., Han, P.L., Hwang, P.M., Feinstein, P.G., Davis, R.L., and Reed, R.R. (1992). The *Drosophila* learning and memory gene rutabaga encodes a $Ca2^{+}$/calmodulin-responsive adenylyl cyclase. Cell *68*, 479–489.

Lin, H.H., Lai, J.S., Chin, A.L., Chen, Y.C., and Chiang, A.S. (2007). A map of olfactory representation in the *Drosophila* mushroom body. Cell *128*, 1205–1217.

Liu, X., and Davis, R.L. (2009). The GABAergic anterior paired lateral neuron suppresses and is suppressed by olfactory learning. Nat. Neurosci. *12*, 53–59.

Liu, C., Plaçais, P.Y., Yamagata, N., Pfeiffer, B.D., Aso, Y., Friedrich, A.B., Siwanowicz, I., Rubin, G.M., Preat, T., and Tanimoto, H. (2012). A subset of dopamine neurons signals reward for odour memory in *Drosophila*. Nature *488*, 512–516.

Louis, T., Stahl, A., Boto, T., and Tomchik, S.M. (2018). Cyclic AMP-dependent plasticity underlies rapid changes in odor coding associated with reward learning. Proc. Natl. Acad. Sci. USA *115*, E448–E457.

Mao, Z., and Davis, R.L. (2009). Eight different types of dopaminergic neurons innervate the *Drosophila* mushroom body neuropil: anatomical and physiological heterogeneity. Front. Neural Circuits *3*, 5.

Maviel, T., Durkin, T.P., Menzaghi, F., and Bontempi, B. (2004). Sites of neocortical reorganization critical for remote spatial memory. Science *305*, 96–99.

Pech, U., Revelo, N.H., Seitz, K.J., Rizzoli, S.O., and Fiala, A. (2015). Optical dissection of experience-dependent pre- and postsynaptic plasticity in the *Drosophila* brain. Cell Rep. *10*, 2083–2095.

Pohl, J.B., Baldwin, B.A., Dinh, B.L., Rahman, P., Smerek, D., Prado, F.J., 3rd, Sherazee, N., and Atkinson, N.S. (2012). Ethanol preference in *Drosophila* melanogaster is driven by its caloric value. Alcohol. Clin. Exp. Res. *36*, 1903–1912.

Poort, J., Khan, A.G., Pachitariu, M., Nemri, A., Orsolic, I., Krupic, J., Bauza, M., Sahani, M., Keller, G.B., Mrsic-Flogel, T.D., and Hofer, S.B. (2015). Learning enhances sensory and multiple non-sensory representations in primary visual cortex. Neuron *86*, 1478–1490.

Prokop, A., and Meinertzhagen, I.A. (2006). Development and structure of synaptic contacts in *Drosophila*. Semin. Cell Dev. Biol. *17*, 20–30.

Saalfeld, S., Cardona, A., Hartenstein, V., and Tomancak, P. (2009). CATMAID: collaborative annotation toolkit for massive amounts of image data. Bioinformatics *25*, 1984–1986.

Schindelin, J., Arganda-Carreras, I., Frise, E., Kaynig, V., Longair, M., Pietzsch, T., Preibisch, S., Rueden, C., Saalfeld, S., Schmid, B., et al. (2012). Fiji: an open-source platform for biological-image analysis. Nat. Methods *9*, 676–682.

Schlief, M.L., and Wilson, R.I. (2007). Olfactory processing and behavior downstream from highly selective receptor neurons. Nat. Neurosci. *10*, 623–630.

Schmid, A., Hallermann, S., Kittel, R.J., Khorramshahi, O., Frölich, A.M., Quentin, C., Rasse, T.M., Mertel, S., Heckmann, M., and Sigrist, S.J. (2008). Activity-dependent site-specific changes of glutamate receptor composition *in vivo*. Nat. Neurosci. *11*, 659–666.

Silva, B., Niehage, C., Maglione, M., Hoflack, B., Sigrist, S.J., Wassmer, T., Pavlowsky, A., and Preat, T. (2020). Interactions between amyloid precursor protein-like (APPL) and MAGUK scaffolding proteins contribute to appetitive long-term memory in *Drosophila melanogaster*. J. Neurogenet. *34*, 92–105.

Tanaka, N.K., Tanimoto, H., and Ito, K. (2008). Neuronal assemblies of the *Drosophila* mushroom body. J. Comp. Neurol. *508*, 711–755.

Tempel, B.L., Bonini, N., Dawson, D.R., and Quinn, W.G. (1983). Reward learning in normal and mutant *Drosophila*. Proc. Natl. Acad. Sci. USA *80*, 1482–1486.

Thévenaz, P., Ruttimann, U.E., and Unser, M. (1998). A pyramid approach to subpixel registration based on intensity. IEEE Trans. Image Process. *7*, 27–41.

Thum, A.S., Jenett, A., Ito, K., Heisenberg, M., and Tanimoto, H. (2007). Multiple memory traces for olfactory reward learning in *Drosophila*. J. Neurosci. *27*, 11132–11138.

Tully, T., Preat, T., Boynton, S.C., and Del Vecchio, M. (1994). Genetic dissection of consolidated memory in *Drosophila*. Cell *79*, 35–47.

Wang, Y., Mamiya, A., Chiang, A.-S., and Zhong, Y. (2008). Imaging of an early memory trace in the *Drosophila* mushroom body. J. Neurosci. *28*, 4368–4376.

Warth Pérez Arias, C.C., Frosch, P., Fiala, A., and Riemensperger, T.D. (2020). Stochastic and arbitrarily generated input patterns to the mushroom bodies can serve as conditioned stimuli in *Drosophila*. Front. Physiol. *11*, 53.

Yasuyama, K., Meinertzhagen, I.A., and Schürmann, F.W. (2002). Synaptic organization of the mushroom body calyx in *Drosophila melanogaster*. J. Comp. Neurol. *445*, 211–226.

Zheng, Z., Lauritzen, J.S., Perlman, E., Robinson, C.G., Nichols, M., Milkie, D., Torrens, O., Price, J., Fisher, C.B., Sharifi, N., et al. (2018). A complete electron microscopy volume of the brain of adult *Drosophila melanogaster*. Cell *174*, 730–743.e22.

STAR★METHODS

KEY RESOURCES TABLE

REAGENT or RESOURCE	SOURCE	IDENTIFIER
Antibodies		
Mouse monoclonal anti-synapsin	DSHB	Cat#3C11; RRID:AB_528479
Rabbit polyclonal anti-RFP	Rockland	Cat#600-401-379; RRID:AB_2209751
Rabbit monoclonal anti-GFP	Invitrogen	Cat#G10362; RRID:AB_2536526
Mouse monoclonal anti-β-Galactosidase	Abcam	Cat#ab116; RRID:AB_298194
Alexa Fluor568-conjugated goat anti-mouse	Life Technologies	Cat#A11004; RRID:AB_2534072
Alexa Fluor488-conjugated goat anti-rabbit	Life Technologies	Cat#ab150077; RRID:AB_2630356
Alexa Fluor568-conjugated goat anti-rabbit	Life Technologies	Cat#A-11011; RRID:AB_143157
Alexa Fluor633-conjugated goat anti-mouse	Life Technologies	Cat#A21050; RRID:AB_141431
Chemicals, peptides, and recombinant proteins		
11-cis vaccenyl acetate (cVA)	Cayman Chemicals	Cat#10010101; CAS:6186-98-7
Geranyl acetate (GA)	Sigma-Aldrich	Cat#W250910-100G-K; CAS:105-87-3
Cycloheximide (CHX)	Sigma-Aldrich	Cat#C4859; CAS: 66-81-9
Carmine	Sigma-Aldrich	Cat#1159330025CAS: 1390-65-4
Experimental models: organisms/strains		
D. melanogaster: MB247-Dα7::GFP,UAS-brp-short^{cherry}	Kremer et al., 2010	N/A
D. melanogaster: R37H08-Gal4	Bloomington Drosophila Stock center	BDSC 49970; FlyBase: FBti0135337
D. melanogaster: P{w[+mC] = UASp-Venus.GAP43}10	Bloomington Drosophila Stock center	BDSC 30896; FlyBase: FBti0129930
D. melanogaster: P{ry[+t7.2] = IArB}rut [2080];P{w[+mC] = UAS-rut.Z}2	Bloomington Drosophila Stock center	BDSC 9405 FlyBase: FBti0038655 FBti0003267
D. melanogaster: P{UAS-GCaMP3.homer}	Pech et al., 2015	FlyBase: FBtp0180847
D. melanogaster: P{UAS-tdTomato.S}2	Bloomington Drosophila Stock center	BDSC 36327; FlyBase: FBti0145103
D. melanogaster: MB247-Dα7::GFP	Kremer et al., 2010;	FlyBase: FBtp0069947
D. melanogaster: UAS-brp-short^{cherry}	Kremer et al., 2010	FlyBase: FBal0286209
Software and algorithms		
Prism7.01	GraphPad	https://www.graphpad.com/scientific-software/prism/
Definiens Developer XD^{TM}	Definiens Inc.	https://www.astrazeneca.com/sustainability.html
TREES toolbox	Cuntz et al., 2010	https://www.treestoolbox.org/
Amira	Zuse Institute Berlin, Thermo Fischer Scientific	https://www.thermofisher.com/us/en/home/industrial/electron-microscopy/electron-microscopy-instruments-workflow-solutions/3d-visualization-analysis-software/amira-life-sciences-biomedical.html
Fiji/ImageJ	Schindelin et al., 2012	https://imagej.net/Fiji

RESOURCE AVAILABILITY

Lead contact

Further information and requests for resources and reagents should be directed to and will be fulfilled by the lead contact, Gaia Tavosanis (gaia.tavosanis@dzne.de)

Materials availability

All stable reagents generated in this study are available from the lead contact upon request.

DATA AND CODE AVAILABILITY

The electron microscopy dataset analyzed in this study was generated in Zheng et al. (2018).

The Definiens™ script used in this study for microglomeruli detection and analysis is available from the Lead Contact on request.

EXPERIMENTAL MODEL AND SUBJECT DETAILS

Flies were raised at 25°C, 60% relative humidity in a 12h/12h light-dark cycle on a standard cornmeal-based diet and collected 0-4d after eclosion for experiments. Behavioral experiments were performed on mixed populations of female and male adult flies. Brains of adult females were dissected for immunohistochemistry and calcium imaging experiments. The fly stocks used in this work were *R37H08-Gal4* (Kind gift of Y. Aso, HHMI, Janelia), *P{UASp-Venus.GAP43}10* (Bloomington *Drosophila* Stock center), *P{UAS-tdTom.S}2* (Bloomington *Drosophila* Stock center), *P{ry[+t7.2] = IArB}rut[2080]* (Han et al., 1992), *P{UAS-GCaMP3.homer}* (Pech et al., 2015), *MB247-Dα7::GFP* (Kremer et al., 2010) and *UAS-brp-short^{cherry}* (Kremer et al., 2010).

METHOD DETAILS

Behavior

All experimental steps were performed at 23°C, 60% relative humidity using mixed populations of *Drosophila* males and females maintained in a 12h/12h light/dark cycle. Flies were collected 0-4d after eclosion, starved for 24 hours on wet paper tissue (Kimberly-Clark Worldwide Inc.) allowing for water uptake and then trained. In appetitive memory experiments ~80 flies were first exposed to an odor (CS-) alone (2min in short- and 5 minutes in long-term memory experiments). After a 2min inter-stimulus pause flies were trained by receiving dry sucrose on filter paper (3M Chr, Whatman) paired with a second odor (CS+) (2min in short- and 5 minutes in long-term memory experiments). 5 minutes of sugar availability improved the survival of flies undergoing the LTM paradigm. In mock controls, all stimuli used in the associative conditioning experiment were presented separately. Flies were tested after 1min retention time for short- or after 24h retention time for long-term memory. During the 24h retention flies were deprived of food and maintained in tubes containing moist paper tissue. During the test flies were allowed to choose between CS+ and CS- odors in a T-maze for 2min. Odors used for conditioning were 11-*cis* vaccenyl acetate (Cayman Chemicals) 1:400 in 5% EtOH in PBS, geranyl acetate (Sigma Aldrich) 1:100 in 5% EtOH in PBS or 5% EtOH in PBS. EtOH was necessary to provide a food-related context to the starved flies (Figure S2B).

De-novo protein synthesis inhibition

Immediately after training, flies were fed 35 mM cycloheximide (Sigma-Aldrich) (Tully et al., 1994) dissolved in 125mM sucrose and 0.01% carmine solution for 30min. The red dye carmine allowed confirming rapid drug uptake. A control group fed with 125mM sucrose and 0.01% carmine (Sigma-Aldrich) solution showed no learning defects.

Immunohistochemistry

2-5 flies were randomly picked from conditioning experiments right before testing. Brains of females were dissected in cold phosphate-buffered saline (PBS) with 0.05% Triton and subsequently fixed in PBS containing 4% formaldehyde at RT for 50 min. After fixation brains were washed in PBS with 0.3% Triton before incubation overnight at 4°C with the following primary antibodies all diluted in PBS with 0.3% Triton: rabbit anti-RFP (1:2000; Rockland), rabbit anti-GFP (1:200; Life Technologies), mouse monoclonal anti-synapsin (3C11, 1:100; DSHB), mouse monoclonal anti-β-Galactosidase (1:200 Abcam). After washing, the brains were incubated with secondary antibodies in PBS containing 0.3% Triton for 4h at RT.

The secondary antibodies were Alexa Fluor568-conjugated goat anti-rabbit, Alexa Fluor488-conjugated goat anti-rabbit, Alexa Fluor568-conjugated goat anti-mouse, Alexa Fluor633-conjugated goat anti-mouse (all used 1:200 and from Life Technologies). Brains were mounted in Vectashield (Vector) and imaged with a laser scanning confocal microscope (LSM 780, Zeiss). For high resolution scans we used a C Plan-Apochromat 63x/1,4 Oil objective (Zeiss; https://www.micro-shop.zeiss.com/?s=1087224394abbdd&l=en&p=us&f=o&a=v&m=s&id=421782-9900-000) with a voxel size of 0.09x0.09x0.25μm^3 for quantitative analysis. Overviews of entire brains were taken with an LCI Plan-Apochromat 25x/0.8 objective (Zeiss) at a voxel size of 0.55x0.55x1μm^3.

To analyze axon and bouton distribution in the calyx, membrane-tagged Venus was expressed in addition to the previously used markers under the control of a DA1-PN Gal4-driver line (*R37H08-GAL4, UAS-Gap43::Venus / MB247-Dα7::GFP, UAS-brp-short^{cherry}*). Brains of 10 female flies per condition were immunolabelled with anti-synapsin antibodies (as above) and imaged. For PN axon reconstruction a high-resolution scan (0.09x0.09x0.25μm^3, 63x NA1.4 oil immersion) of the right brain hemisphere of female flies was acquired with a confocal microscope. In addition, an overview scan used for registration was taken with a low magnification objective (25x; NA 0.8 multi-immersion).

Two-photon *in vivo* calcium imaging

A mixed population of up to 4d old *MB247-homer::GCaMP3* flies were starved for 18h at 22°C before appetitive conditioning with cVA (1:400, 5% EtOH in PBS), GA (1:100, 5% EtOH in PBS) was used as CS-. Starved untrained flies displayed no bias toward either of these odors at 24 hours. Flies used for imaging were randomly picked from the trained group right before testing. They were used for imaging only if the remaining flies from the same group had learned. For imaging, flies were briefly anesthetized on a Peltier element at 4°C, placed into a custom-built imaging chamber (Figure 4A) and fixed using adhesive tape. The head capsule was opened under Ringerś solution (5 mM HEPES, pH 7.4, 130 mM NaCl, 5 mM KCl, 2 mM $CaCl_2$, 2 mM $MgCl_2$). To minimize movement brains were stabilized with 1,5% low melting agarose (Thermo Scientific) in Ringerś solution. Flies were imaged with a two-photon laser-scanning microscope (LaVision BioTec, TriM Scope II) equipped with an ultra-fast z-motor (PIFOC® Objective Scanner Systems 100μm range) and a Zeiss C-Apochromat 40x, 1.1 NA water –immersion objective. Two-photon images were analyzed using Fiji/ImageJ (Schindelin et al., 2012). GCaMP fluorescence was excited at 920 nm using a Ti:sapphire laser (Coherent Chameleon). A stack consisting of ~10 optical sections was taken at 1Hz in approximately 0,26x0,26μm xy- and at 4μm z- resolution. Odors were applied with a constant humidified air stream (10ml/s) using a commercial device (Stimulus Controller CS 55, Ockenfels SYNTECH GbmH) triggered 5 s after acquisition of the 1st frame by a multifunction I/O module (NI USB-6008), which was controlled by MATLAB (Data Acquisition Toolbox). To record DA1 neurons specific responses, *UAS-tdTomato; R37H08-GAL4, MB247-Homer::GCaMP3* flies were anesthetized on ice, positioned in a polycarbonate imaging chamber (Louis et al., 2018), and immobilized using Myristic Acid (Sigma-Aldrich). To allow optical access to the Calyx, a small window was opened through the head capsule under Ringerś solution. Two-photon microscopy was conducted as described above.

QUANTIFICATION AND STATISTICAL ANALYSIS

EM reconstruction and identification

Neuron skeletons were reconstructed in a serial section transmission electron microscope (ssTEM) volume of a complete female adult *Drosophila melanogaster* brain (Zheng et al., 2018) and manually traced using CATMAID (Saalfeld et al., 2009). Thus, traced neuron skeletons represent the branching of neurons and the location of their cell bodies and synapses. Chemical synapses were manually annotated and identified consistently with the criteria of other CATMAID-based *Drosophila* connectomic studies (Zheng et al., 2018): 1) an active zone (AZ) surrounded by vesicles, 2) a presynaptic specialization (e.g., T-bar), 3) synaptic cleft and 4) a post synaptic density zone (PSD), which however can be absent. If the PSD is absent, we annotated all cells along the synaptic cleft as postsynaptic (Zheng et al., 2018, Prokop and Meinertzhagen, 2006). Neuron identity is based on previously described morphologies in light microscopy (KC subtypes, APL, MB-C1, PN), such as dendritic branching, axonal projection and location in the neuropil (Aso et al., 2014, Tanaka et al., 2008, Liu and Davis, 2009, Grabe et al., 2015, Jefferis et al., 2007). Additionally, we performed a neuron search against a light microscopy dataset in NBLAST (Costa et al., 2016), as described in Zheng et al. (2018) for PN subtype identification. 3D reconstructions of the PN bouton and KC claws from ssTEM sections were created manually with the ImageJ plugin TrakEM2 (Cardona et al., 2012).

Behavior

A performance index (PI) was calculated as the ratio of the difference between the number of flies that chose the CS+ and those that chose the CS- odor and the total number of flies: $PI = \frac{(CS+)-(CS-)}{(CS+)+(CS-)}$.

Axon reconstruction

PN axon reconstruction was performed on the high-resolution scan of Venus signal in the trees toolbox available for MATLAB (Cuntz et al., 2010). In a second step, tracings and high-resolution images were aligned to the registered calyx. For generation of a standard calyx with a volume of 37583 μm^3 (Figure 3E, light green) the Dα7 signal of three registered calyces was averaged and reconstructed in Amira using the segmentation editor. Next, tracings were aligned to the registered overview scan in two steps. First, the iACT of the high-resolution image and of the registered brain in the Venus channel were aligned. Next, the calyx volume of the high-resolution calyx and the standard calyx went through a rigid registration performed in Amira. The alignment parameters were then applied to the axon reconstructions. Boutons were traced on the now registered high-resolution images with the landmark function in Amira. Bouton distribution inside the MBC was evaluated within a 3D grid of 10 μm^3 cubes.

Two-photon image data processing

The time series was processed with a custom Fiji/ ImageJ macro and corrected for small x/y shifts with the StackReg plug-in (Thévenaz et al., 1998). A grid (ROIs, side length 5 μm) was assigned for each optical slide of a stack covering the entire calyx. Intensity tables of each square of the grid were exported to Microsoft Excel and the ΔF/F was calculated. The baseline (F_0) was set by averaging the intensities within each ROI of the 5 frames prior to odor stimulation. ROIs were regarded as responsive, if their normalized ΔF/F% throughout the first 2 s of odor application exceeded 3x the standard deviation of the F_0 of the same ROI in the 5 s (= 5 images) before odor stimulation. The 3x standard deviation threshold was chosen as it provided the suitable sensitivity for the evaluation of odor-elicited responses without introducing excessive noise. ROIs below that threshold were assigned into the category

"unresponsive." ROIs calcium responses higher than the threshold were further subdivided into three categories. The first category was "Carrier" (responsive to both, 5% EtOH and 1:400 cVA, 5% EtOH). The second category was "cVA" (responsive only to 1:400 cVA, 5% EtOH and not to 5% EtOH) or "EtOH" (response only to 5% EtOH application and not to 1:400 cVA, 5% EtOH). To analyze DA1 boutons responses to 5% EtOH and 1:400 cVA+ 5% EtOH were recorded from naive *UAS-tdTomato; R37H08-GAL4, MB247-Homer::GCaMP3* flies, exported to Fiji/ ImageJ and ROIs were manually drawn around DA1 boutons based on the tdTomato fluorescence. Intensity values of each ROI were transferred to Microsoft Excel and ΔF/F values were calculated using the average of the first 5 frames prior to odor stimulation as baseline (F_0). Responsive ROIs were defined as above. These results were age, gender and sequence independent as presenting the odors in a different order did not change the results of the analysis. Calcium traces were generated in Prism 7 (GraphPad Software).

Statistics

Statistical analyses were performed with Prism7.01 software (GraphPad). All data were tested for normality (D'Agostino & Pearson omnibus normality test) and homogeneity of variances (F-test). Comparisons of normally distributed data were tested by a one-sample t test, a two-sample t test or one-way analysis of variance (ANOVA) followed by planned, pairwise multiple-comparison tests with adjusted p values (Bonferroni). Definition of statistical significance was set to < 0.05. Asterisks denote * $p < 0.05$; ** $p < 0.01$; ***$p < 0.001$; **** $p < 0.0001$; n.s. not significant. All experimental tests performed and their relative p values are reported in Table S2.

Cell Reports, Volume *34*

Supplemental information

Circuit reorganization in the *Drosophila* mushroom body calyx accompanies memory consolidation

Lothar Baltruschat, Luigi Prisco, Philipp Ranft, J. Scott Lauritzen, André Fiala, Davi D. Bock, and Gaia Tavosanis

Supplementary Figures

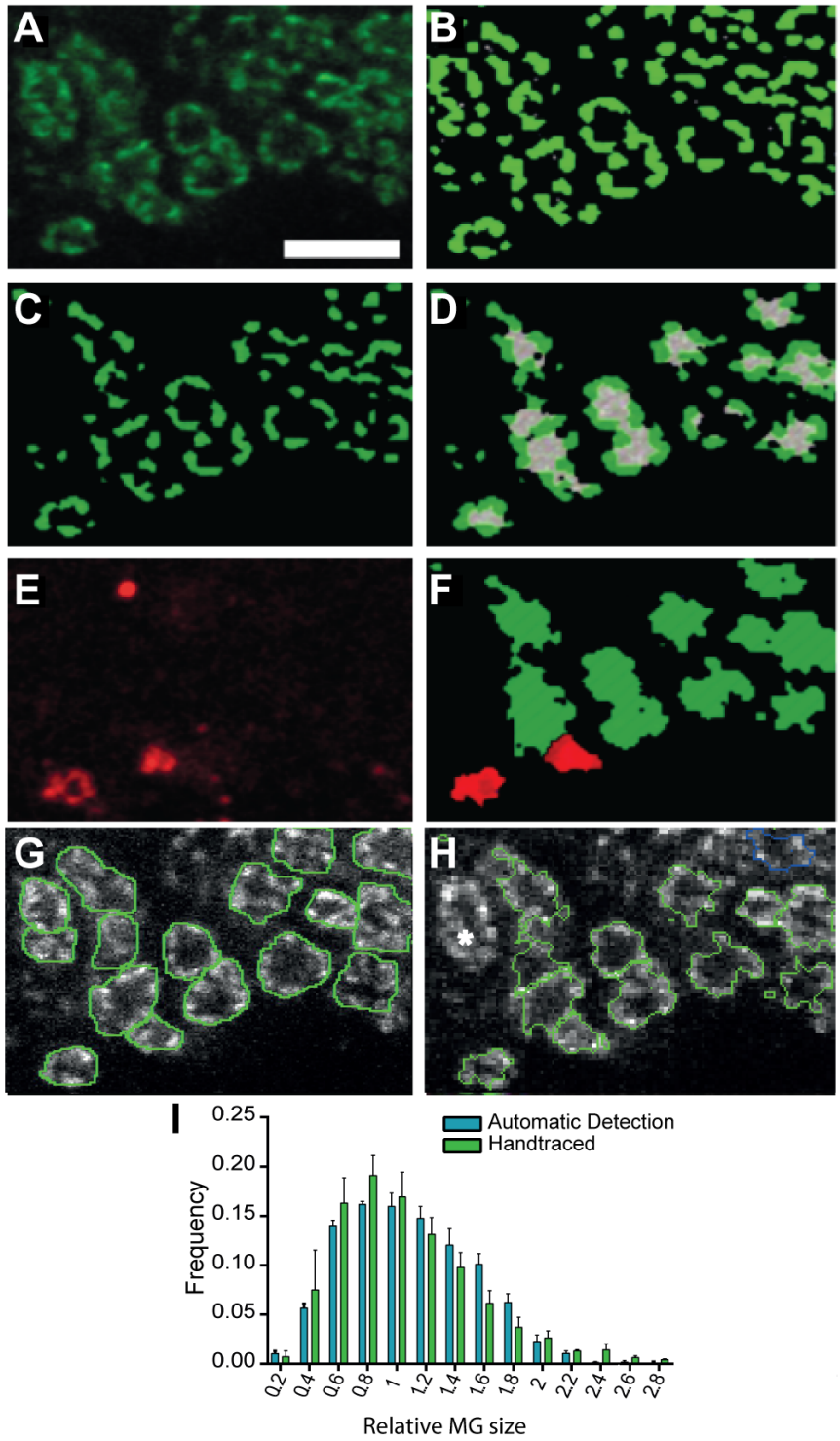

Figure S1| Automated identification and reconstruction of microglomeruli (Related to Figure 1)

(A) Example of a small area from a typical optical section used for the automated detection. Only the green channel containing the Dα7 signal was used for identification of MGs. An anisotropic filter was applied to the original image and contrast was enhanced. Scale bar = 5 µm. **(B)** Initial segmentation of the entire image was performed by grouping pixels with similar grey values into individual objects (green). **(C)** A membership function assigned by applying a histogram shape-based threshold on the brightest objects of this contrast map as candidate objects for MG rings (dark green). **(D)** A second threshold was set to assign seed points for MG lumen within darkest areas surrounded by MG ring candidates. These seed lumen candidate objects grew in a watershed analysis 1 pixel for 5 cycles in 3D into dark areas or until a MG ring candidate object was reached. Lumen candidate objects were classified as "real lumen" (grey) by a fuzzy classification approach depending on lumen candidate volume, their elliptic fit (or roundness) and their relative border with ring candidate objects. Final MG rings (light green) were finally detected in 3D by watersheding into bright areas using the lumens as seed points. **(E)** The red channel containing the Brp-short^{cherry} signal was applied to create objects representing labelled active zones. **(F)** MGs identified in the green channel image that colocalized with the independently generated objects in the red channel image were classified as R37H08-positive (DA1- MGs; red). MGs that did not colocalize with Brp-short^{cherry} signal were displayed in green. **(G)** To evaluate the performance of the routine, all MGs within 4 MBCs were traced manually (green rings) and were overlaid in a custom Matlab script with automatic reconstruction. **(H)** Result of the comparison of the automated and the manual reconstruction shown in (G). MGs detected in the manual reconstruction and in the automated reconstruction are displayed in green ("*correct*"). These were 59% of all manual-counted MG. MGs only detected in the automated reconstruction ("*false-positive*") are displayed in blue and represented ~3.7% of the detected MGs. Additional possible errors of the reconstruction were "*undersegmented*", if multiple MG were fused in the automated reconstruction compared to the manual reconstructions (~2.4% of the detected MGs) and "*false-negative*", if a MG was detected only in the manual reconstruction. **(I)** Comparison of the size distribution of MG detected manually (green) or by the software (blue) in the same optical sections. Comparison of the relative size distribution frequencies with Kolmogorov-Smirnov test revealed no significant difference between manual and automated MG identification ($p>0.5$, $n=4$).

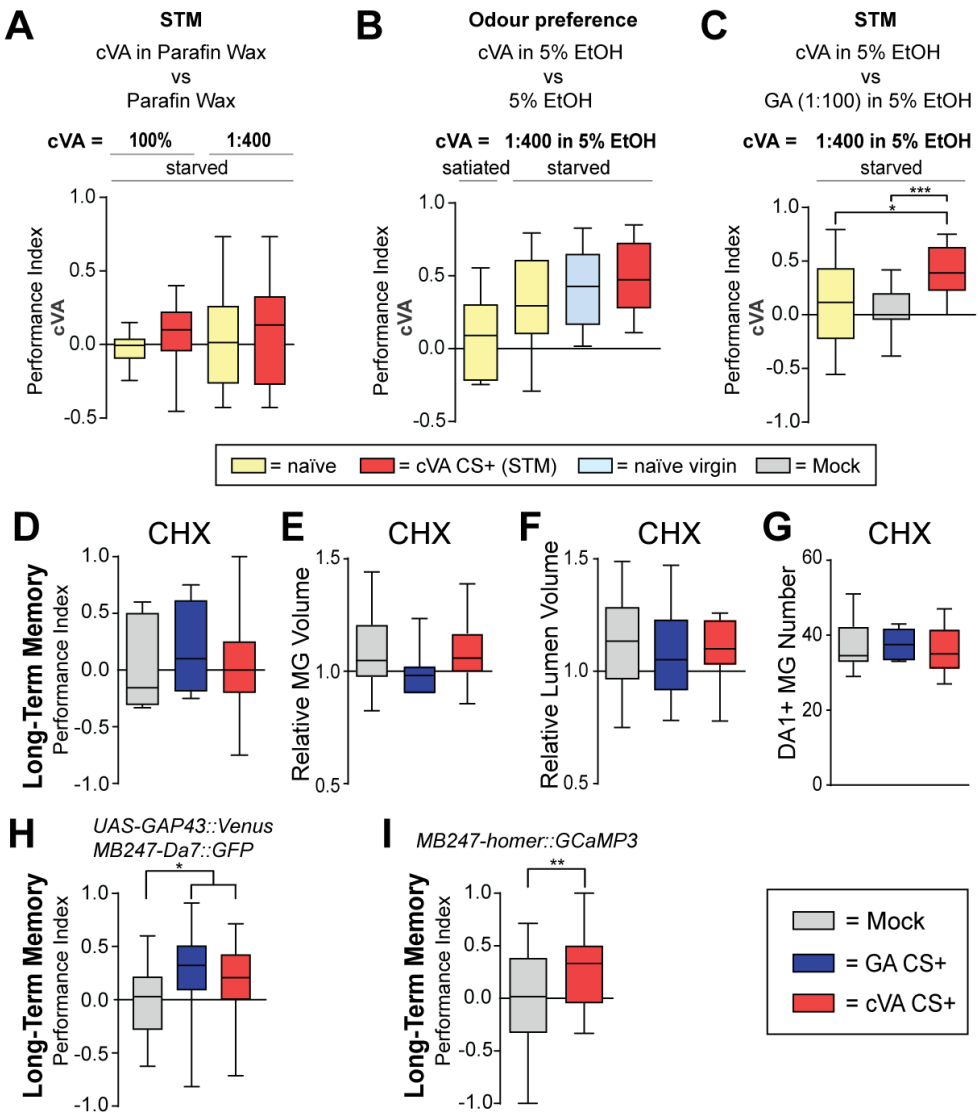

Figure S2| Establishment of appetitive conditioning with cVA, suppression of anatomical modifications after pharmacological blocking of long-term memory (Related to Figure 2) and learning scores of individual genotypes (Related to Figures 3, 4)

(A) Appetitive STM conditioning using pure cVA or cVA diluted 1:400 in paraffin wax induced performance scores towards cVA that were similar to those of naïve flies ($p > 0.05$, n = 8-16). **(B)** The pheromone cVA was attractive for naïve flies when applied in a food context (choice: 1:400 cVA + 5% EtOH versus 5% EtOH). Attraction was stronger if flies were starved, if virgin females were tested or after appetitive conditioning using cVA (1:400 in 5% EtOH) as CS+ and the carrier (5% EtOH) as CS- ($p > 0.05$, n = 9-19). **(C)** Comparison of performance scores towards cVA of flies that were confronted with the choice between cVA (1:400 in 5% EtOH) and GA (1:100 in 5% EtOH). Flies that had been trained in an appetitive STM paradigm with cVA (1:400 in 5% EtOH) as CS+ and GA (1:100 in 5% EtOH) as CS-

displayed higher performance scores towards cVA in comparison to mock-trained flies or starved naïve flies, indicating that flies can learn to associate cVA with a reward in these conditions (*p < 0.05, ***p < 0.001, n = 12-19). **(D)** Pharmacological suppression of LTM by feeding *R37H08-GAL4/ UAS-brp-short^{cherry}, MB247-Dα7::GFP* flies 50 mM cycloheximide (CHX) in 125mM sucrose solution for 30 min after training. Subsequently flies were re-starved for 24h before testing (p > 0.05, n = 8–11). **(E-G)** Suppression of the structural modifications in DA1- MGs in cVA CS+ flies after LTM block by CHX application. (p > 0.05, n = 7-17). Compare to Figure 2G-I. **(H)** Appetitive LTM scores of *R37H08-Gal4, UAS-GAP43::Venus /MB247-Dα7::GFP, UAS-brp-short^{cherry}* flies (*p < 0.5, n= 23-32), used in Figure 3A-H. **(I)** Appetitive LTM scores of *MB247-homer::GCaMP3* flies (**p < 0.01, n = 32-34), used in Figure 4A-F and in Figure S3. In all box plots, the edges of the boxes are the first and third quartiles, thick lines mark the medians, and whiskers represent data range.

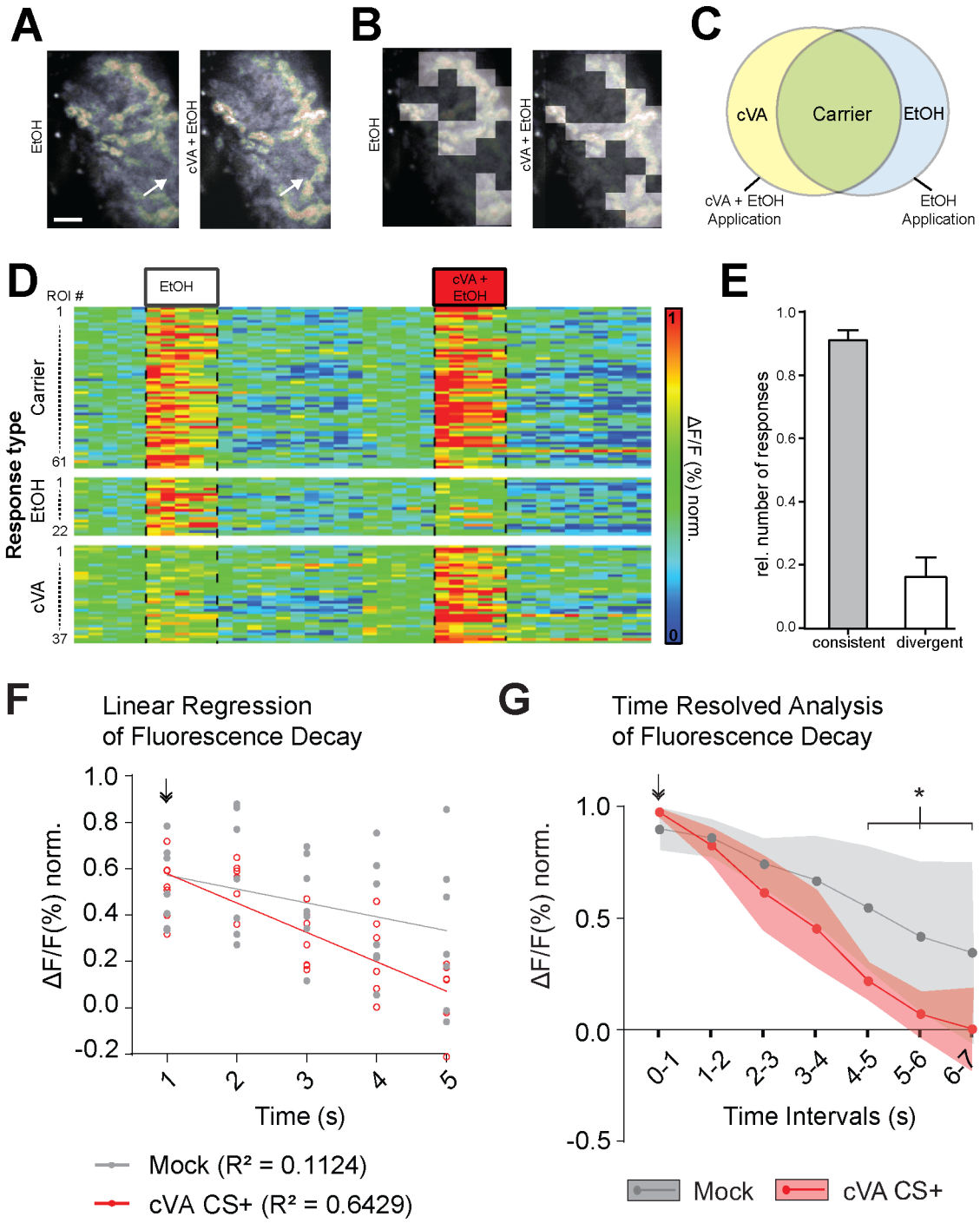

Figure S3| Classification of calcium responses in the MBC (Related to Figure 4)

(A) Representative optical section of a time z-stack series consisting of 30 cycles with 10 sections per stack at a frame rate of 1 Hz. The odour was applied for 5s after 5 cycles. With a typical calycal diameter along the dorsal/ventral axis of 35µm and an average MG diameter of 5µm this imaging settings reliably captured calcium dynamics of the entire MBC. The grey scale image was created by averaging images from one optical plane over the last 15 acquisition cycles after odour application. False color-coded images were created by subtracting the background (generated by averaging 5 images preceding the odour

application) from the first two averaged images during odour application. White arrows point to areas only responsive to cVA. Scale bar = 10 µm **(B)** Single optical planes were overlaid with a grid of 5x5 μm^2 meshes (ROIs). White squares represent ROIs, which were classified as responsive to odour stimulation. For classification the mean response as ΔF/F% during the first 2s of odour application was calculated for each ROI. ROIs were classified as odour responsive, if the mean ΔF/F% during the first 2s of odour application was greater than 3x the standard deviation of the ΔF/F% during the 5s preceding odour stimulation. **(C)** Schematic of ROI classification strategy. ROIs were classified as responsive to “cVA” if they displayed an above-threshold response to cVA (1:400, 5% EtOH), but not to EtOH only (5% EtOH). “Carrier” ROIs responded to both stimuli and “EtOH” only to EtOH (5% EtOH), but not to cVA (1:400, 5% EtOH). **(D)** Temporal dynamics of fluorescence changes to odour stimulation within a single MBC. Each lane of the matrix represents a single ROI identified as responsive towards the carrier (top matrix), EtOH only (mid matrix) or cVA (bottom matrix) as in (C). Each column of the matrix represents 1s. White and red boxes and dashed lines represent 5s of odour stimulation with 5% EtOH or cVA (1:400, 5% EtOH), respectively. Out of 120 responsive ROIs in one MBC, 61 ROIs were classified as responsive to the carrier, 22 to EtOH and 37 were specific to cVA. **(E)** Number of consistent responses (ROI present in trial 1 that are also detected in trial 2) in the MBC after repetitive odour stimulation with 5% EtOH. After two consecutive odour stimulations ~90% of the responsive areas kept consistent compared to a previous stimulation (n = 6). The fraction of ROIs only responsive during 2nd odour stimulation, and classified as divergent, was ~16%. **(F)** Comparison of calcium signal decay in KC dendrites by linear regression analysis. From its peak after the start (arrow) of five seconds stimulation with cVA, calcium response decays more rapidly in cVA CS+ trained flies than in mock trained flies. A linear fit described the decrease of GCaMP fluorescence well in cVA CS+ trained flies, whereas decay was less homogenous in flies from the mock trained group. ($p < 0.05$, n = 7). **(G)** Time resolved analysis of fluorescence decay of GCaMP after the initial peak. During the initial two seconds of cVA stimulation (arrow) average responses in KC dendrites reached their peak in each condition. The calcium response was undistinguishable between the two groups until 3-4 s of stimulation, but it decayed more rapidly from 4-5 s on in the cVA CS+ flies (*$p < 0.05$, n = 7). Data represented as mean ± std.

Connection to DA1-PN bouton	Cell type	Number of cells	Number of synaptic connections
Postsynaptic to the DA1-PN bouton	KC αβp	0	0
	KC αβc	1	12
	KC αβs	3	11-21
	KC α'β'ap	1	25
	KC α'β'm	1	8
	KC γmain	8	12-24
	KC γd	0	0
	APL	1	2
	MB-C1	2	1-3
Presynaptic to the DA1-PN bouton	KC γmain	2	1
	APL	1	3
	MB-C1	1	1

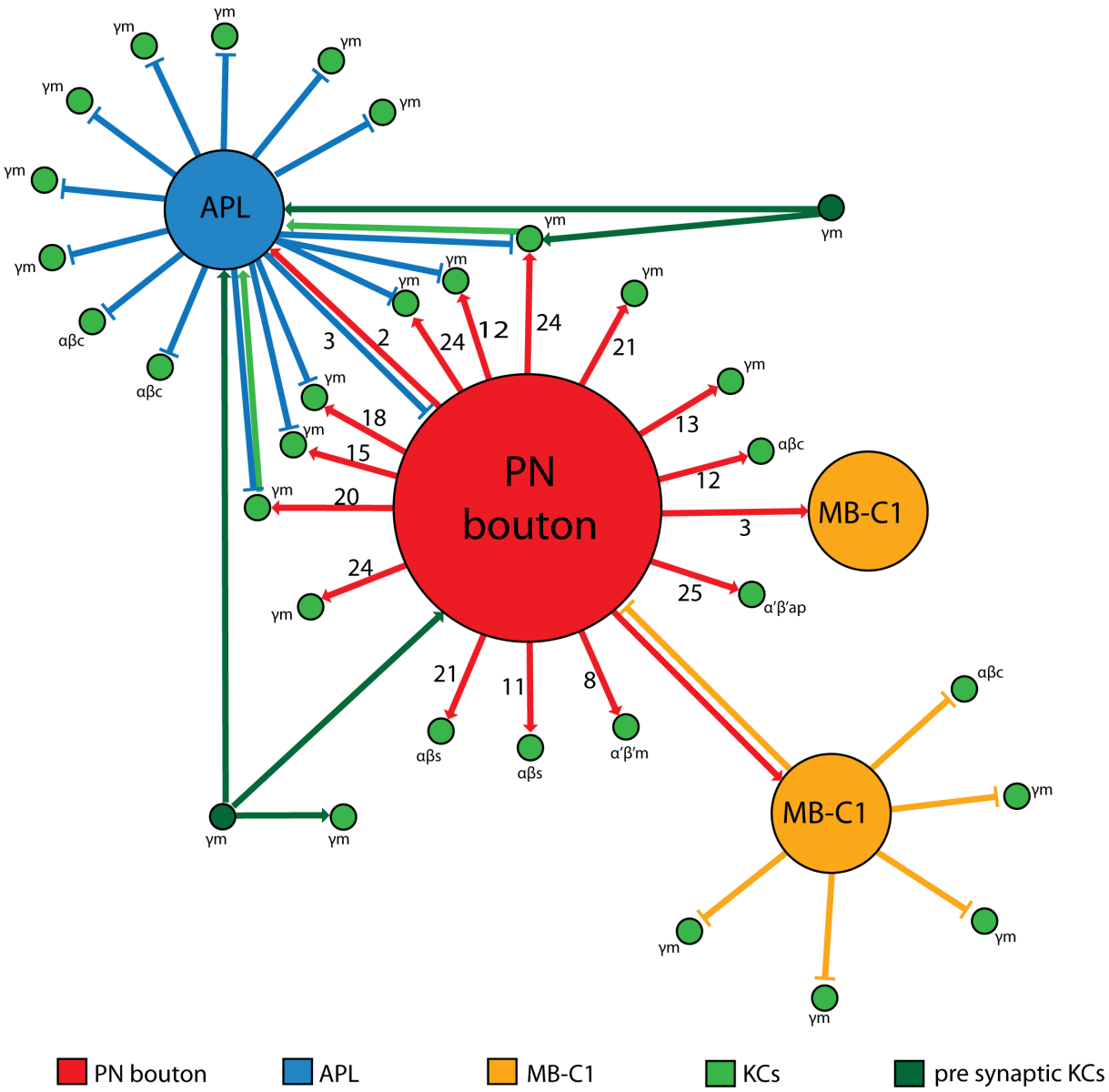

Supplementary Table1| Neurons contributing to a DA1-PN microglomerulus and their synaptic connections (Related to Figure 1)

Top: Table representing the identified direct synaptic contacts between the DA1-PN bouton (see Figure 1) and other neurons, revealed from reconstructions in the FAFB EM dataset. Bottom: Scheme of the MG network of the DA1-PN bouton (see Figure 1) reconstructed in the FAFB EM dataset. If synaptic connections are more than one, their number is indicated along the arrows. The network consists of a DA1-PN bouton (red), surrounded by the APL neuron (blue), two MB-C1 neurons (orange), 14 postsynaptic KC claws and two additional KCs (dark green), which are presynaptic to the PN bouton and to APL. APL and MB-C1 form polyadic synapses with the PN bouton including KCs. Some of these are not postsynaptic to the PN bouton and are therefore placed in the scheme around the respective APL or MB-C1 neuron.